Available online at www.sciencedirect.com

jmr&t Journal of Materials Research and Technology

journal homepage: www.elsevier.com/locate/jmrt

Original Article

Influence of thermomechanical treatment on the shape memory effect and pseudoelasticity behavior of conventional and additive manufactured Fe–Mn–Si–Cr–Ni-(V,C) shape memory alloys

Maryam Mohri [a], *Irene Ferretto* [a], *Hesamodin Khodaverdi* [b], *Christian Leinenbach* [a,c,*], *Elyas Ghafoori* [d]

[a] *Empa, Swiss Federal Laboratories for Materials Science and Technology, Dübendorf, 8600, Switzerland*
[b] *School of Metallurgy and Materials Engineering, College of Engineering, University of Tehran, Tehran, Iran*
[c] *Laboratory for Photonic Materials and Characterization, École Polytechnique Fédérale de Lausanne (EPFL), 1015, Lausanne, Switzerland*
[d] *Institute for Steel Construction, Faculty of Civil Engineering and Geodetic Science, Leibniz University Hannover, 30167 Hannover, Germany*

ARTICLE INFO

Article history:
Received 7 March 2023
Accepted 20 April 2023
Available online 25 April 2023

Keywords:
Fe-based shape memory alloy
Pseudoelasticity
Training
Shape memory effect
4D printing
Metal AM

ABSTRACT

This study evaluated the influence of heat treatment and thermomechanical training on the microstructural evolution and mechanical characteristics of conventional and additive-manufactured FeMnSi-based shape memory alloys. The conventional samples were produced by casting and rolling. The additive-manufactured samples were manufactured using the laser powder bed fusion (L-PBF) technique. Both specimens were subjected to the same heat treatment and thermomechanical training. The heat treatment involved solution annealing at 1050 °C for 2 h and aging at 750 °C for 6 h, and the thermomechanical training concluded with a 4% elongation at ambient temperature followed by annealing at 250 °C for 15 min. This training cycle was repeated four times for each sample after heat treatment. The heat treatment improved the pseudoelasticity and shape memory effect of the samples. Although training further enhanced the pseudoelasticity, it also reduced the shape memory effect. Thermomechanical training led to the formation of a large number of stacking faults, which facilitated the inverse phase transformation of martensite (ε) to austenite (γ) during unloading, resulting in improved pseudoelasticity. The heat-treated additive-manufactured samples showed the highest total recovery strain owing to the pseudoelasticity and shape memory effect. This characteristic could be due to the smaller grain size and higher volume fraction of precipitates. The precipitates and grain refinement improved the conditions for partial dislocation motion by increasing the back stresses on the martensite tip.

* Corresponding author. Empa, Swiss Federal Laboratories for Materials Science and Technology, Dübendorf, 8600, Switzerland.
E-mail address: Christian.Leinenbach@empa.ch (C. Leinenbach).

https://doi.org/10.1016/j.jmrt.2023.04.195

Nomenclature

SMAs	Shape memory alloys
Fe-SMA	Iron-based shape memory alloy
PE	Pseudoelasticity
SME	Shape memory effect
AM	Additive manufacturing
3D	Three-dimensional
4D	Four-dimensional
PBF	Powder bed fusion
L-PBF	Laser powder bed fusion
XRD	X-ray diffraction
SEM	Scanning electron microscope
TEM	Transmission electron microscopy
HCP	Hexagonal close-Packed
FCC	Face-centered-cubic
ε_{pe}	Pseudoelastic strain
ε_{el}	Elastic strain
ε_{ul}	Unloading strain
ε_{rec}	Recovery strain
σ_Y	Yield strength
E	Young's modulus
A_s	Austenite start formation temperature
A_f	Austenite finish formation temperature

1. Introduction

Shape memory alloys (SMAs) are among the most important types of functional materials because of their pseudoelasticity (PE) and shape memory effect (SME) [1,2]. The SME occurs when a deformed material can regain its primary shape after heating, and PE is defined as the recovery of considerable strain after unloading. Among the different SMAs, NiTi- and Fe-based SMAs have gained considerable attention owing to their unique properties, PE, and SME. The former alloy is known for its excellent PE and SME, while the good mechanical properties (e.g., workability and high strength) and inexpensive production cost of the latter are highlighted [3–6]. SMAs display tremendous potential for sensors and actuators or tensioning and damping structures in various fields, such as aerospace and civil infrastructure [7–9].

NiTi SMAs have recently been exploited as energy-absorption members [10] and seismic isolators [10]. The production cost of NiTi alloys has been an obstacle to the widespread application of this material, particularly in civil engineering domains where large amounts of the material are usually required. Fe–Mn–Si-based SMAs have become significant SMAs since 1982, when the perfect SME in an Fe–30Mn–Si(%wt.) alloy was discovered by Sato et al. [11]. Fe–Mn–Si-based SMAs have gained considerable attention owing to their good SME, weldability, machinability, mechanical properties, and inexpensive production [4], which justify their application in civil engineering. In particular, the alloy has been used for pre-stressed strengthening of civil infrastructure [12], girders [13], connections [14], and historic bridges [15].

Nevertheless, limited studies (e.g. Refs. [16,17]) have investigated the use of Fe-based SMAs as energy-dissipation elements. It has been reported that although Fe-based SMAs have a suitable energy dissipation capability and low-cycle fatigue performance, they do not display appropriate PE [17], resulting in unfavorable residual deformation in structures after loading.

Extensive investigations of Fe-based SMAs were performed more than fifteen years ago. Finally, an Fe–Si–Mn-based SMA including nano-sized VC was designed and patented by Empa [18,19]. This alloy was mainly designed to present a good SME (and not PE) that can be applied for the pre-stressed strengthening of civil infrastructure. A stress-induced martensitic transformation from the austenite (FCC-γ) phase to the martensite (HCP-ε) phase during loading and its inverse phase transformation (ε to γ) during unloading at room temperature lead to the PE effect. The inverse phase transformation (ε to γ) after heating above the austenite start temperature (A_s) causes the SME in Fe-based SMAs [11]. The effects of the grain size, texture, precipitates [28], and orientation of grains [20,27] on the phase transformation have been studied extensively, along with the alloy reaction under cyclic loading–unloading, performance, and creep [21]. These studies have shown that although this Fe-based SMA has a good energy dissipation capability, it offers only negligible PE [22]. However, there many studies have explored the SME of this alloy; its PE has been scarcely investigated to date [19,23–25]. Previous research has illustrated that special textures and VC precipitates can improve the PE [18,19,26–29]. Recent studies have indicated that grain refinement and precipitation of VCs lead to enhanced PE. In addition, thermomechanical treatment reduced the formation of thermal twins and created a [111] texture in the austenite matrix, which decreased the critical stress for inducing the martensite transformation [28]. It has been further reported that thermomechanical treatment could enhance the SME of Fe–Mn–Si-based alloys [19,28,30–32]. This thermomechanical treatment involves inducing a small deformation at room temperature, which causes the formation of stress-induced martensite, followed by annealing above the A_f, finish austenite formation temperature, to induce the reverse martensitic transformation. An uncomplicated thermomechanical training of an Fe–Mn–Si SMA that involved deformation at 600 °C followed by annealing at 800 °C was reported to lead to enhanced PE behavior at temperatures around 100 °C. The formation of stacking faults (SFs) and reversible movement of related partial dislocations improved the PE [33].

To date, Fe-based SMAs have been fabricated using conventional manufacturing technologies such as casting, forging, and hot or cold rolling [19]. Additive manufacturing (AM) or 3D printing is a collection of advanced manufacturing methods based on adding materials layer-by-layer to build the final part. As a result, AM has been recognized as an attractive alternative for the fabrication of parts with intricate 3D geometries [34]. Four-dimensional (4D) printing is a procedure by which a 3D-printed structure changes its shape, properties, and functionality under external energy, such as light, temperature, or other environmental stimuli [35]. SMA structures can recover their initial shape after applying stress or deformation and subsequent heating, and thus they are known as 4D printed structures. Owing to the simplicity of fabrication

and achievable complexity of printed parts, 4D printing, as a novel subdivision of AM, has been used to manufacture various functional devices [36,37].

The laser powder bed fusion (L-PBF) process, which uses powdered materials as feedstock and a laser as the heat source, is known to be very beneficial for processing complex and lightweight structures. Studies have indicated that L-PBF with optimized parameters could offer good mechanical characteristics that are sometimes improved compared to the same alloy fabricated by traditional processes such as hot working or casting [38].

Previous studies have shown that the microstructure, and consequently the mechanical behavior and transformation temperatures of SMA parts, are affected by process parameters and can change because of the influence of the heat source on the material composition. The studies offered some solutions, e.g., optimizing the process parameters, to improve the manufacturability of SMAs [39,40].

AM of an Fe–Mn–Al–Ni alloy by L-PBF with proper PE was reported by Niendorf et al. [41]. The Fe–Mn–Ni–Al alloy was investigated for the fabrication of lattice structures with PE performance. It was found that the alloy contained coarse grains with both austenitic and martensitic phases. The recovery strain of the bulk material was 1.3%, whereas the lattice displayed a recovery strain of approximately 2%. Nevertheless, the alloy was prone to cracking through L-PBF, and preheating at 500 °C was necessary to produce specimens without cracks [42]. Recent studies by Ferretto et al. [43,44] indicated that a complex 3D geometry of Fe–17Mn–5Si–10Cr–4Ni (%wt.) SMA could be produced by L-PBF. The optimal volumetric energy density (VED) and laser scan velocity for L-PBF, relevant microstructures, and mechanical properties were reported in these studies. In addition, AM samples exhibit enhanced SME and PE compared with conventionally manufactured alloys having the same composition [45]. The phase transformation behavior of this AM Fe-based SMA was also evaluated by Kim et al. [46]. The results indicated that the primary ferrite (BCC-δ) phase formed during manufacturing because of the fast cooling rate and rapid solidification. Ferretto et al. [44] reported that selective Mn evaporation during L-PBF could change the volume phase fraction of the ferrite (BCC-δ) and austenite (FCC-γ) phases. In addition, the δ to γ phase transformation induced by the intrinsic heat treatment refined the microstructure and decreased the crystallographic texture.

The Fe–Mn–Si SMA containing nano-sized VC developed at Empa is used as a raw material for the AM process in this study. Currently, this alloy is used as strips and rods at an industrial scale. The influence of various heat treatments on the microstructure, SME, and PE under both conventional manufacturing and AM of the Fe–Mn–Si SMA containing VC has been reported in previous studies [25,29,45,47]. It was reported that an aging treatment at 750 °C for 6 h provided the maximum PE in both the conventionally manufactured and AM samples [28,45]. However, there have been no studies on the influence of thermomechanical treatment on AM Fe-based SMAs. Therefore, the purpose of this study is to investigate and compare the SME, PE behavior, and energy absorption capability of conventionally manufactured and AM Fe-based SMAs with the same composition after heat and thermomechanical treatments.

2. Experimental procedure

2.1. Conventional Fe-based SMA

A conventional Fe-based SMA that was induction-melted in air and hot-rolled was provided by re-fer AG for this research. The chemical composition was Fe–17Mn–5Si–10Cr–4Ni-1(V, C) (%wt.). Dog-bone-shaped specimens were fabricated from sheets with a thickness of 1.5 mm using electrical discharge machining (EDM). The dog-bone-shaped geometry and dimensions are shown in Fig. 1. This as-received conventional material is designated as AC.

The as-received specimens were subjected to heat treatment followed by thermomechanical training. The treatment involved solution-annealing at 1050 °C for 2 h, followed by aging at 750 °C for 6 h and air-cooling. These samples are referred to as HC.

The heat-treated samples underwent the following training treatment: tensile loading up to 4% strain at ambient temperature, followed by heating at 250 °C for 15 min. This thermomechanical cycle was repeated four times. The conventional samples subjected to thermomechanical treatment are designated as THC.

2.2. Additive manufactured Fe-based SMA

The Fe-based SMA powder was provided by Bohler Edelstahl-Kapfenberg-Austria and was fabricated by gas atomization in an Ar atmosphere from a conventional alloy to obtain spherical particles with an average size of 33 μm. A Sisma MySint 100 L-PBF machine (Sisma S.p.A., Italy) with a 1070 nm fiber laser and a spot size of 55 μm was used to fabricate the AM samples in an argon environment. The applied output power was 175 W, and the scanning strategy was bidirectional without border contour, followed by a rotation of 90° between the layers. Based on a previous study [43] on a similar alloy, applying a high VED can lead to the formation of dense parts without fusion defects or cracks. The optimized parameters used for the fabrication of blocks were a scanning speed of 225 mm/s, laser power of 175 W, layer thickness or 0.03 mm, and hatch spacing of 0.1 mm [48]. Dog-bone-shaped tensile specimens with a loading direction perpendicular to the build direction were cut using EDM. The geometry and dimensions of the AM specimens were similar to those of the conventional specimens (Fig. 1). The same heat and thermomechanical

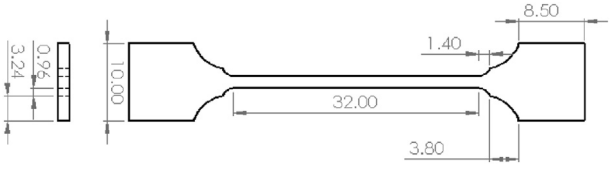

Fig. 1 – Dimensions and geometry of the tensile dog-bone-shaped specimens (dimensions in mm).

treatments as for the conventional specimens were applied to the AM specimens. The AM samples were subjected to solution annealing to dissolve the precipitates and ferrite phase. Table 1 summarizes the heat and thermomechanical treatments for both the conventional and AM samples.

2.3. Microstructure and phase investigation

The phase components were characterized by X-ray diffraction (XRD) (Bruker-D8) with Cu-Kα radiation using a Ni filter with a thickness of 0.012 mm at 200 mA and 45 kV. Microstructural characterization was performed using scanning electron microscopy (SEM; FEI NanoSEM230) and FEI Tecnai F20 series transmission electron microscopy (TEM). Samples for SEM observation were polished and etched with a solution of H_2O_2 (35%), HNO_3 (65%), and HCl (32%) at a ratio of 7/30/9. TEM specimens were prepared using standard electropolishing. The electrolytic solution was perchloric acid and ethanol (1:9), used at −20 °C and 22 V.

2.4. Thermo-mechanical tests

The Tensile tests were performed using a universal tensile testing machine (Z020, Zwick/Roell). In these tests, the specimens were loaded to a strain of 4% and unloaded to a constant force of 10 N at a constant displacement rate of 0.5 mm/min. The recovered strain due to PE (ε_{pe}) was measured by subtracting the elastic strain (ε_{el}) from the total recovery strain variation after unloading (ε_{ul}) as follows:

$$\varepsilon_{pe} = \varepsilon_{ul} - \varepsilon_{el} \quad (1)$$

2.4.1. Recovery strain

Activation processes were performed on all samples to measure the recovery strain. After subjecting the samples to a pre-strain of 4%, heating the sample leads to the recovery of a part of the residual pre-strain due to the SME of the Fe-based SMA, which is called the "recovery strain." It is important to note that recovery strain can be achieved when the sample moves freely back to its primary shape. A Zwick machine with a climate-controlled chamber was used to measure the recovery strain of the pre-strained samples. The samples were subjected to a constant preloading of approximately 5 N during the heating and cooling cycles. Then, the temperature was increased from 23 °C to 200 °C at a rate of 3 °C/min. The specimens were held at 200 °C for 30 min, followed by cooling to 23 °C at a rate of 3 °C/min. The strains in the samples were continuously recorded using a clip-on extensometer (with a gauge length of 20 mm) during the heating/cooling cycle. The ultimate strain recorded at the end of the test was considered as the recovery strain, $\varepsilon_{rec.}$

3. Results and discussion

3.1. Microstructural characterization

The XRD patterns of the conventional and AM specimens after heat treatment and training are displayed in Fig. 2. The as-received conventional sample is fully austenitic. In contrast, the XRD pattern of the as-built AM sample shows peaks related to γ-austenite, ε-martensite, and δ-ferrite.

Owing to the cyclic heating-cooling followed by rapid cooling of the samples during AM by L-PBF, residual thermal stresses and an ε-martensite phase are induced in the as-built AM samples. Kim et al. [43,46] reported that the primary δ-ferrite phase formed as a result of high cooling rates and rapid solidification. However, solution treatment can dissolve the δ-ferrite phase.

Both α'-martensite and ε-martensite can also be induced in the microstructure by heat treatment or training in the conventional and AM samples. However, more α'-martensite is formed owing to training, and ε-martensite is more expected to be induced by aging. Brake et al. [49] reported that α'-martensite could be nucleated at the intersection of two ε-martensite laths. Therefore, after training, owing to the increase in the number of ε-martensite laths, the probability of their interaction increases, resulting in the formation of α'-martensite.

Fig. 3 displays SEM images of the conventional and AM specimens before and after heat treatment and training. The microstructure of the as-received conventional specimen consists of equiaxed austenite grains with a mean size of 14 μm (Fig. 3a). However, after solution-annealing at 1050 °C for 2 h and aging at 750 °C for 6 h, the austenite grains grow, and the average grain size reaches 60 μm (Fig. 3b). Furthermore, Fig. 3b shows elongation of the precipitates at the grain boundaries and inside the grains– with a length of

Table 1 – List of manufacturing, heat treatment, and thermomechanical treatment processes.

Specimen name	Manufacturing process	Heat treatment[c]	Training treatment[d]
AC[a]	Conventional process		
HC	Conventional process	✓	
THC	Conventional process	✓	✓
AB[b]	Additive manufacturing		
HA	Additive manufacturing	✓	
THA	Additive manufacturing	✓	✓

[a] As-received conventional sample.
[b] As-built additive manufactured sample.
[c] Solution annealing at 1050 °C for 2 h followed by air quenching and aging at 750 °C for 6 h.
[d] Application of tension up to 4% followed by annealing at 250 °C for 15 min.

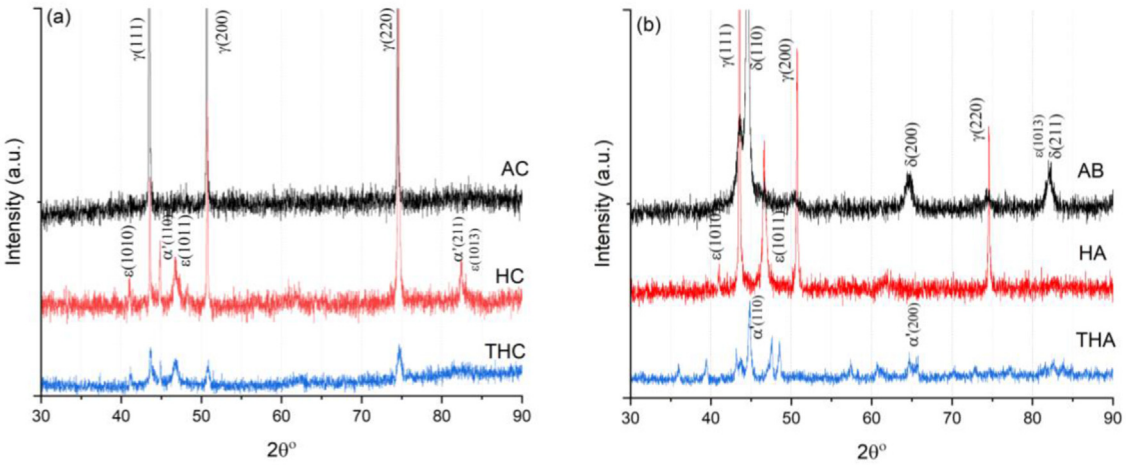

Fig. 2 – X-ray diffraction patterns of (a) conventional and (b) additive manufactured samples before and after heat treatment and thermomechanical training. AC: as-received, HC: heat-treated, and THC: heat-treated + trained conventional samples; AB: as-built, HA: heat-treated, and THA: heat-treated and trained AM samples.

300–500 nm in the heat-treated sample. Two types of precipitates (needle- and polyhedral-shaped) are observed inside the grains. The size and number of precipitates at the grain boundaries are greater than those in the grain interior. After training, parallel lines are present inside the grains. These may be ε-martensite phase, twin, or slip bands (Fig. 3c), which are characteristic of annealed and cold-worked austenitic steels [50].

Fig. 3d illustrates the microstructure of the AM sample after manufacturing (as-built). The microstructure is characterized by three specific features: melt pools, grains, and fine dendritic structures. Similar features were previously reported for other alloys fabricated by L-PBF, such as Al-based alloys [51], austenitic steels [52], and Ni- and Co-based alloys [53].

The melt pools appear as half-spheres (Fig. 3d) and overlap as a result of the layer-by-layer deposition. Two different regions can be distinguished. The melt pool boundaries are decorated by coarser grains because of the melt pool overlap and partial reheating of the previously deposited layers. The interior of the melt pools is characterized by a fine dendritic microstructure with a columnar morphology. Dendrites grow in the direction of the heat flow and toward the center of the laser path [54]. The formation of these fine columnar dendrite structures is associated with the rapid solidification of the molten material during the process, where cooling rates of $10^3 - 10^8$ K/s are achieved [54]. The solidification structure depends on the thermal field near the solid–liquid interface, which defines the local solidification parameters, i.e., the temperature gradient, solidification front velocity, and cooling rate. As the heat flow within the melt pool is particularly complex and the spatial temperature distribution is not homogeneous, changes in the solidification morphology and size are observed within the same melt pool [55].

Solution annealing at 1050 °C for 2 h causes a change in the microstructure of the AM samples. The melt pools, coarse grains, and dendritic structures are no longer visible (Fig. 3e). The heat-treated AM sample (HA) exhibits an approximately fourfold increase in carbides inside the grains with a higher volume fraction (approximately 1×10^8 particles/cm^2) compared with the heat-treated conventional sample (HC) (0.25×10^8 particles/cm^2) after aging at 750 °C for 6 h. The carbide precipitates exhibit a more uniform distribution within the microstructure of the HA sample. Fig. 3e shows that the average grain size is close to 20 μm after the heat treatment. Fig. 3f shows the microstructure of the HA sample after training (THA). Some twin and slip bands or ε-martensite phase bands are observed in the THA sample.

The TEM images of the trained conventional THC and additive-manufactured THA samples, shown in Fig. 4, indicate large amounts of SFs and dislocations in the austenitic (FCC) matrix after training. The formation of carbide precipitates in the microstructure causes lattice distortion, which induces SFs and dislocations, eventually resulting in ε-martensite lath formation [56]. The XRD and TEM results illustrate the presence of ε-martensite and α′-martensite in the heat-treated samples. Brake et al. [49] noted that α′-martensite can be nucleated at the intersection of ε-martensite laths. Similar structural components are observed in both the conventional and AM samples after the training process. An alternative reason for the presence of the observed lines may be the creation of shear bands and annealing twins. Additionally, carbide precipitation forms a heterogeneous stress distribution in the microstructure, which can trigger ε-martensite formation [26]. The selected area electron diffraction (SAED) pattern of the SF-containing region (black circle) shows that a large number of SFs lead to the formation of a large amount of ε-martensite within the microstructure (see Fig. 4a and c). Kajiwara proposed a model in which that SFs behave as nucleation sites for ε-martensite, and a large number of SFs due to lattice strain causes ε-martensite creation to rectify the lattice distortion caused by other precipitates or ε-martensite [57,58]. These SFs are created in certain directions and are bound to the twins and grain boundaries. The SFs and ε-martensite are developed by the high residual stress created during the training process. In the AM sample (Fig. 4f), the length of SFs is shorter than that of the conventional sample, which may be due to the smaller grain size in the AM

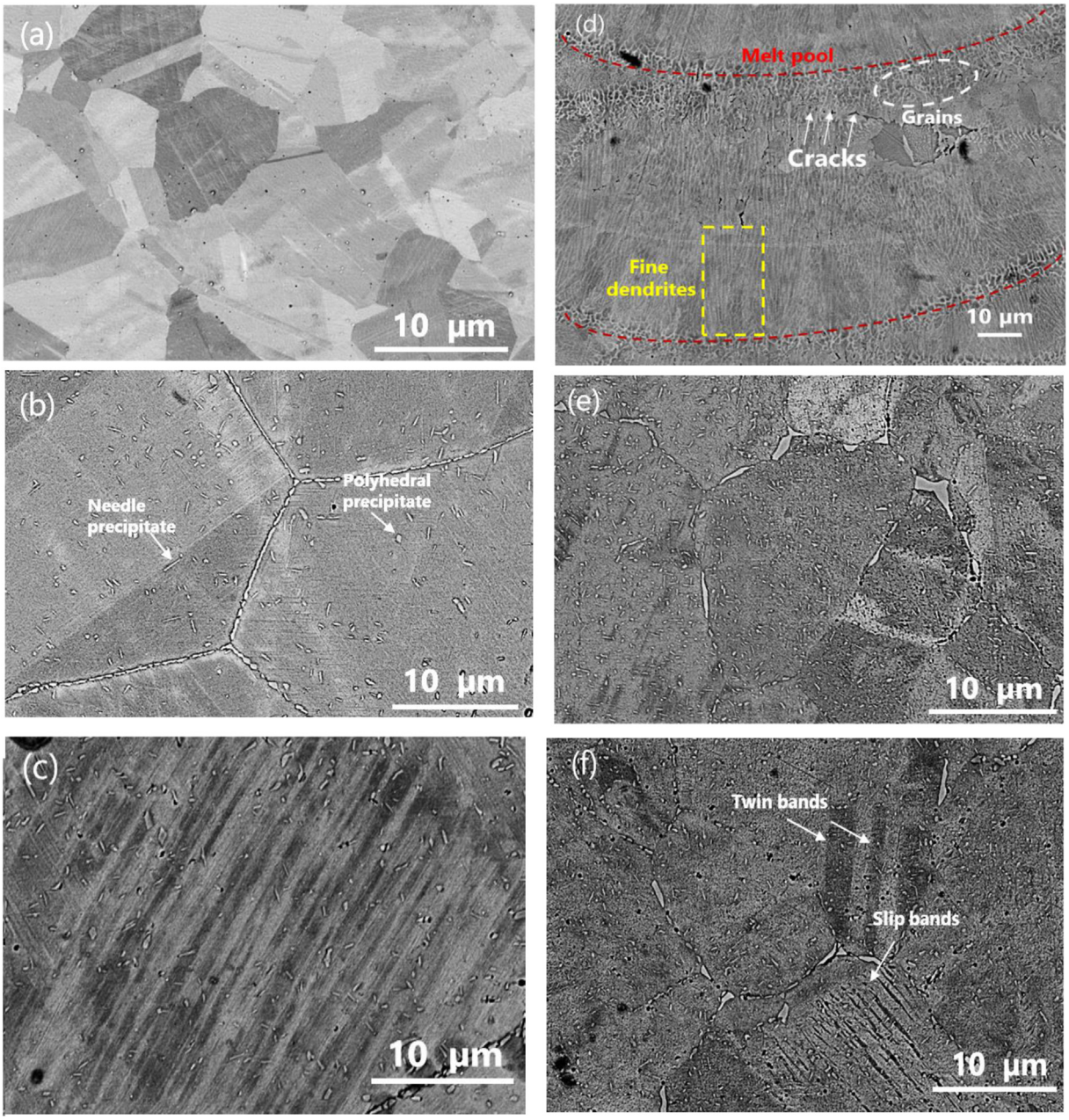

Fig. 3 – SEM images of conventional (a) as-received, (b) heat-treated, and (c) trained samples, and additive manufactured (d) as-built, (e) heat-treated, and (f) trained samples.

sample. After aging, the microstructure contains different precipitates, as shown in Fig. 4a, d, and e. In addition to the needle- and polyhedral-shaped precipitates observed in the SEM images (Fig. 3b), fine nanometer precipitates (~25 nm) ae also observed in the TEM image (Fig. 4e). The internal stress created around the precipitates owing to the lattice mismatch between the matrix and particles leads to an accumulation of strain and the formation of SFs and ε-martensite at the interface [56]. Furthermore, a large number of dislocations are formed in the trained samples because of several loading and unloading cycles, which leads to plastic deformation. During the training, two processes occur: generation of stress-induced martensite (SIM) with multiplication of dislocations through deformation, and the inverse martensitic transformation (ε to γ) with annihilation of dislocations during heating. It is likely that at low-temperature recovery (250 °C), partial annihilation of dislocations occurs, and the stress fields around the unrecovered dislocations facilitate the SIM transformation. Fig. 4d shows the dark-field image of the area containing precipitates and dislocations (red square in Fig. 4a). The results show the interaction between fine precipitates and dislocations. The strain field coherency around the precipitates can interact with the induced dislocations, pin the latter, and consequently lead to their accumulation.

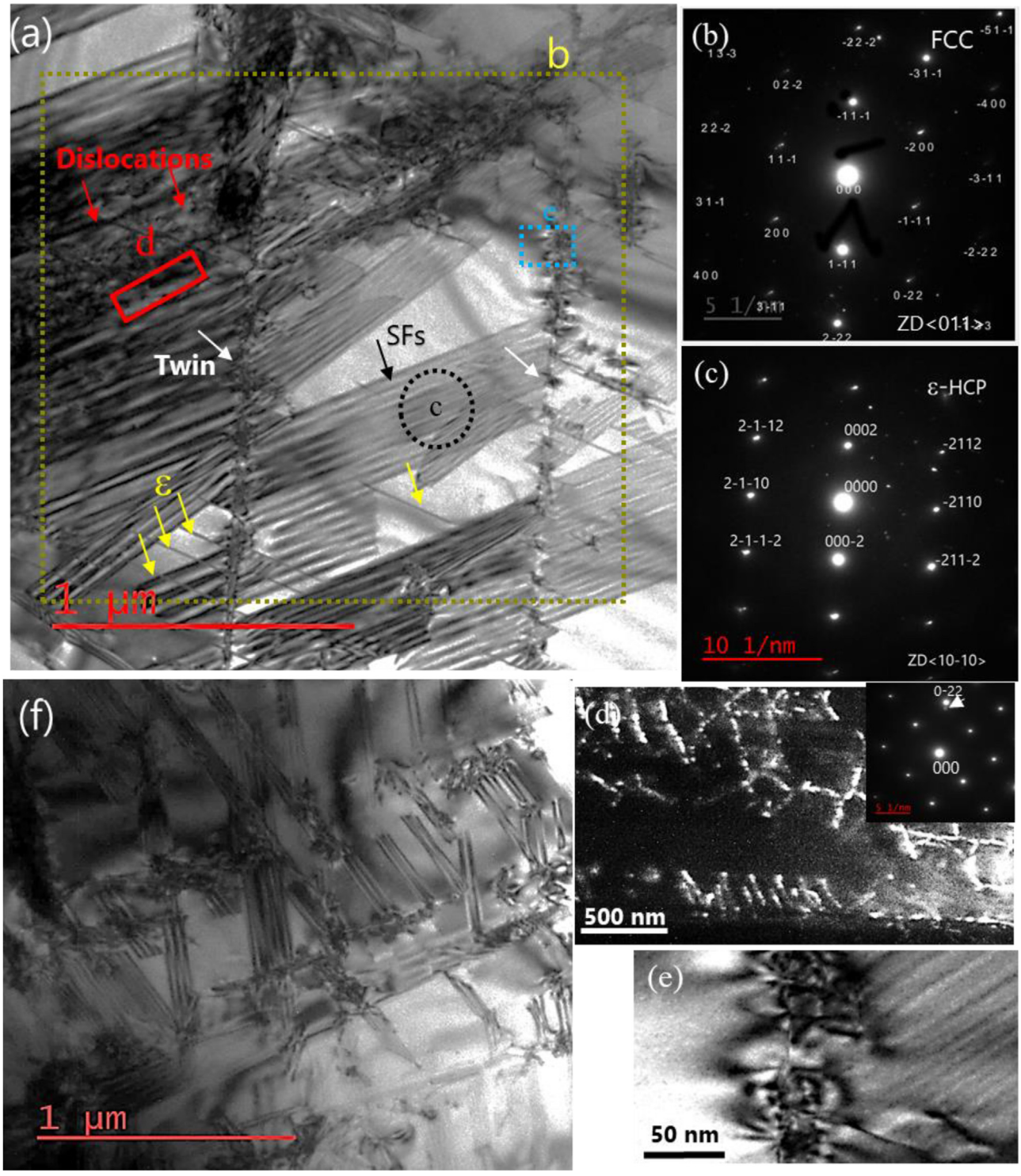

Fig. 4 – TEM analysis of (a) trained conventional sample (THC); selected area electron diffraction patterns (SAED) corresponding to (b) the austenitic matrix and (c) martensite phase; (d) the inset represents the SAED pattern of the austenite and precipitates (shown by small marker) and dark-field image of precipitates; (e) bright-field image of the precipitates, (f) bright-field image of the trained additive manufactured sample (THA) showing the existence of SFs, HCP-ε, and twins.

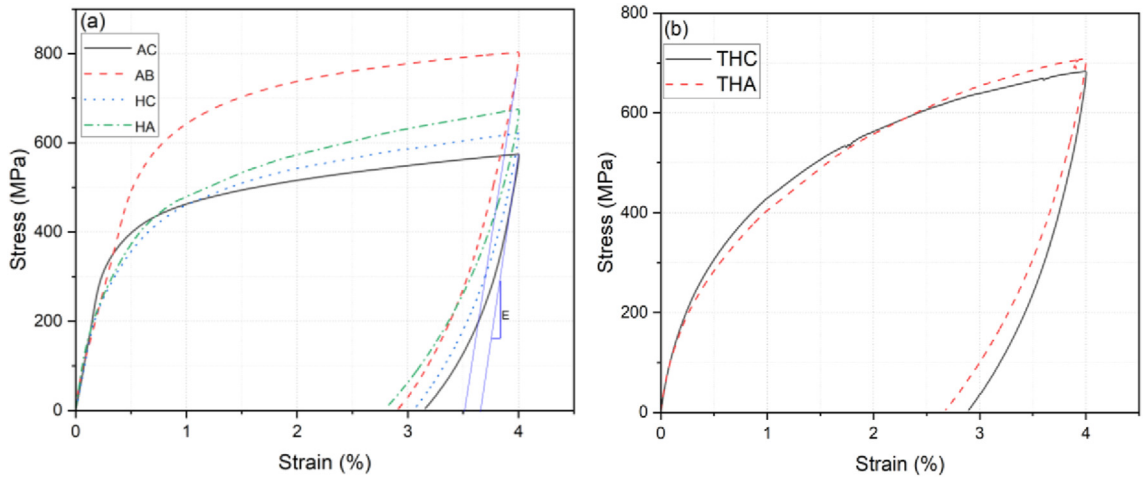

Fig. 5 – Stress–strain curves of conventional and AM specimens after (a) heat treatment and (b) training (AC: as-received, HC: heat-treated, and THC: heat-treated + trained conventional samples; AB: as-built, HA: heat-treated, and THA: heat-treated and trained AM samples).

3.2. *Mechanical behavior*

3.2.1. *Pseudoelasticity and absorbed energy*

The non-linear deformation behavior after elastic deformation during loading is owing to martensitic transformation followed by plastic deformation. Lee et al. [59] reported that a 0.1% yield stress is more appropriate than a 0.2% yield stress for determining the stress start for martensite transformation. Hence, a yield stress of 0.1% ($\sigma_{Y\ 0.1\%}$) is considered in this study.

The tensile test results up to a 4% strain are shown in Fig. 5 for both the conventional and AM samples before and after heat treatment and the training process. The mechanical properties such as the PE (ε_{pe}), Young's modulus, and yield stress of the samples derived from Fig. 5 are listed in Table 2. The as-received conventional (AC) and as-built (AB) AM samples exhibit elastic moduli of 135 and 145 GPa, respectively. The heat-treated conventional and AM samples exhibit elastic moduli of 125 and 166 GPa, respectively. The differences in the elastic modulus may be due to differences in the chemical composition or the amount of martensite and austenite phases in the conventional and AM specimens after heat treatment. After training, the elastic modulus of both heat-treated samples is 125 GPa. It should be mentioned that because of the pronounced non-linear behavior of Fe-SMAs, the elastic modulus measurement is not precise, and it is suggested that the slope of the tangent line to the loading stress–strain curve below 100 MPa is used to measure the elastic modulus.

For both the conventional and AM samples, the 0.1% yield stress decreases after the heat treatment and training, indicating that stress-induced martensite formation occurs more easily. The 0.1% yield stresses of the heat-treated samples are 290 and 258 MPa for the conventional and AM samples, respectively, which indicates that stress-induced martensite formation starts at lower stresses in the AM sample than in the conventional sample. The yield stress of the trained samples is reduced by approximately 100 MPa. By applying thermomechanical treatment, the work hardening is increased (Fig. 5b). The strengths at 4% strain (σ_4%) are 620 and 680 MPa for the heat-treated conventional and AM samples, respectively. However, $\sigma_{4\%}$ is increased to 700 MP after training.

The tensile tests demonstrate that the yield strength decreases after heat treatment. The yield strength of these alloys results from the martensite transformation, which is enhanced by precipitation. The decrease in the yield strength is thus because of precipitate formation and the development of martensite transformation. The higher strain-hardening rate in the heat-treated and trained samples is also due to the increase in the ε-martensite volume fraction and dislocation density caused by aging and training in both the conventional and AM samples [56].

Table 2 – Mechanical properties of conventional and AM samples before and after heat treatment and training (ε_{pe}: pseudoelastic strain, ε_{rc}: recovery strain after heating to 200 °C, ε_{re}: residual strain).

Specimens name	E (GPa)	$\sigma_{Y\ 0.1\%}$ (MPa)	ε_{pe} %	ε_{rc} %	ε_{re} %	Absorbed energy (J/cm^3)
AC	135	360	0.53	0.7	2.44	17.2
HC	125	290	0.60	1.11	1.95	17.8
THC	125	196	0.73	0.51	2.37	17.5
AB	145	408	0.66	0.86	2.05	23
HA	166	258	0.85	0.99	1.89	18
THA	125	180	0.95	0.48	2.17	16.5

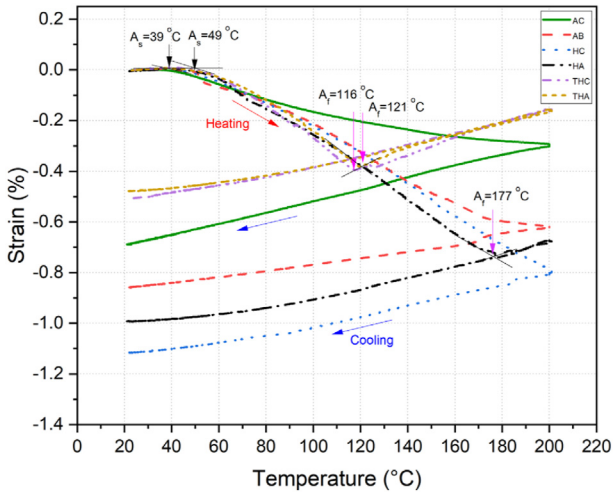

Fig. 6 – Recovery strain as a function of temperature after exposure to 4% strain for conventional and additive manufactured samples; CR: as-received conventional, AB: as-built additive manufactured, CH: heat-treated conventional, CHT: trained heat-treated conventional, AH: heat-treated additive manufactured, AHT: trained heat-treated additive manufactured samples.

The reduction in the Young's modulus after training may be owing to the large number of SFs, as shown in Fig. 4a and f. The existence of carbide precipitates in the austenite and SFs lead to an increased dislocation density in the microstructure. According to Chen et al. [60] and Over et al. [61], the decrease in the Young's modulus is related to the variation in the interatomic bonding structure at the SFs and further dislocation movement, respectively.

The ε_{pe} for the as-received sample is 0.53%, which increases to 0.60% after heat treatment. A comparison with the as-received specimen indicates that the PE strain of the trained specimen increases to 0.73%. A similar trend is observed for the AM samples. The PE strains obtained for the AM samples are 0.66%, 0.85%, and 0.95% for the as-built, heat-treated, and trained samples, respectively. The value of 0.95% is the highest PE strain reported thus far, compared to the maximum of 0.8% reported in a previous study [27]. The amount of absorbed energy upon 4% loading and unloading in the conventional samples is almost constant (approximately 17–18 J/cm^3), but it increases to 23 J/cm^3 in the as-build AM sample and decreases to 18 and 16.5 J/cm^3 with aging and training, respectively.

The AM samples show higher PE strains than the conventional samples, which may be due to the greater number of precipitates and the smaller grain size in the AM samples. The training treatment leads to an increase in PE for both the conventional and AM samples to 0.73% and 0.95%, respectively. However, the absorbed energy after heat treatment and training is almost the same as that of the conventional samples.

3.2.2. *Thermo-mechanical behavior*

To evaluate the recovery strain due to the SME, all of the samples were subjected to a strain of 4% at room temperature followed by an activation process (i.e., heating to 200 °C and cooling to room temperature). Fig. 6 shows the recovery strain as a function of temperature after a strain of 4% for the conventional and AM samples. Generally, the strain curves can be divided into four stages during one cycle of heating and cooling. During heating from room temperature, the strain increases with increasing temperature because of thermal expansion (first stage). With a further increase in the temperature, the martensite to austenite transformation begins above A_s temperature due to the SME and results in a decrease in the strain up to A_f temperature (second stage). Above A_f, the transformation of martensite to austenite is complete, and increasing strain as a result of the further thermal expansion of austenite can be measured (third stage). After cooling, the strain decreases linearly owing to thermal contraction of the samples (fourth stage). Therefore, the A_s and A_f temperatures can be obtained from the strain–temperature curves, as shown in Fig. 5. The measured A_s temperatures for the as-received conventional sample (AC) and as-built AM sample (AB) are 39 and 49 °C, respectively. Heat treatment and training lead to a slight increase in A_s. The A_f temperatures for the as-received and heat-treated conventional samples are greater than 200 °C, but training leads to a decrease to 116 °C. For the AM heat-treated and trained samples, the A_f temperatures are 177 and 121 °C, respectively. Hence, the results show that training leads to a further decrease in the A_f temperature.

Moreover, the results indicate that the heat-treated conventional and AM samples (HC and HA) have higher recovery strains than the trained samples. However, the AM samples present a higher PE, but the recovery strain of the heat-treated conventional sample is higher than that of the heat-treated AM sample. Nevertheless, the recovery strains of the trained samples are almost the same for both conventional and AM samples. Therefore, training improves PE but reduces the strain recovery due to the SME. Deformation at room temperature not only results in the formation of ε-martensite but also in a certain amount of SFs and dislocation gliding, i.e., irreversible plastic strain. Some of the ε-martensite phase formed owing to the SIM transformation during loading can be recovered to γ-austenite (i.e., PE), and more can return during heating (i.e., SME). Furthermore, high amounts of SFs induce the inverse martensitic transformation (i.e., PE). Therefore, the amount of residual ε-martensite after unloading decreases, and subsequently, the strain recovery decreases after heating.

The reduction in residual strain is due to enhanced reversibility from the martensite phase to the austenite phase during unloading and heating. Lai et al. [56] considered that the improvement in reversibility after aging was due to the generation of very fine single variant martensite (less than 3 nm) induced by strain against the very thick and multi-variant martensite plates that prevail in the free state of the precipitates. The heat-treated AM sample exhibits the lowest residual strain or highest total recovery strain owing to the PE and SME. This characteristic may be due to the smaller grain size and higher volume fraction of precipitates. In addition, this indicates a more pronounced transformation of austenite to ε-martensite and vice versa because of the higher mobility of the Shockley partial dislocations. Grain refinement and

carbide precipitates enhance the motion of partial dislocations by increasing the back stresses.

As reported by Ming et al. [62], decreasing the average grain size increases the austenite phase strength, which in turn inhibits ε-martensite generation along dissimilar orientations inside the grain. This situation decreases the chance of ε-martensite phases intersecting with each other to provide an opportunity for α′-martensite formation.

Thermomechanical training increases the amount of ε-martensite, thereby improving the PE in both the conventional and AM samples. On the other hand, it increases the probability of martensite lath interactions and causes the formation of α′-martensite at the intersections of the lathes. Therefore, the residual martensite laths after unloading have less mobility and reversibility to the austenite phase, which results in a decrease in the recovery strain after heating (SME). However, grain refinement in the AM samples decreases the probability of ε-martensite intersection, which in turn reduces the possibility of α′-martensite formation.

4. Conclusion

This study evaluated the influence of heat treatment and thermomechanical training on the microstructural evolution and mechanical properties of conventional and additive-manufactured FeMnSi-based SMA (Fe–17Mn–5Si–10Cr–4Ni–1(V–C) wt.%). The heat treatment consisted of solution annealing at 1050 °C for 2 h and aging at 750 °C for 6 h. Thermomechanical training was conducted with tension up to 4% strain, followed by annealing at 250 °C for 15 min, and this cycle was repeated four times for each sample after heat treatment. Based on the experimental results and detailed microstructural and mechanical characterization, the following conclusions were drawn.

1. Heat treatment of conventional and additive-manufactured samples resulted in a microstructure consisting of a uniform distribution of carbide precipitates that led to the generation of a high density of SFs and ε-martensite laths within the microstructure.
2. Thermomechanical training led to the formation of a microstructure consisting of austenite grains, stacking faults, carbide precipitates, and thin ε-martensite laths with partial dislocation arrays. Compared to the as-received conventional or as-built additive-manufactured microstructures, the training resulted in a reduction in the Young's modulus and an increase in the $\sigma_{4\%}$ due to easing the $\gamma \rightleftharpoons \varepsilon$ transformation through loading unloading. These changes led to an increase in the pseudoelasticity of both samples.
3. Additive-manufactured samples showed higher pseudoelasticity and lower residual strain (after activation) than the conventional specimens after heat treatment and training. The enhanced performance of the AM samples was correlated to the specific microstructure produced during the L-PBF procedure. The rapid cooling and thermal cycling applied to the samples led to the creation of a special microstructure in the as-built samples, which contained smaller grains compared with conventional samples and affected the interaction between ε-martensite lathes and the grain boundaries.
4. The heat-treated additive-manufactured sample displayed the lowest residual strain or the highest total recovery strain owing to PE and SME. This characteristic could be due to the smaller grain size and higher volume fraction of precipitates. Indeed, the grain refinement and carbide precipitates enhanced the motion of partial dislocations by increasing the back stresses.

Declaration of competing interest

The authors declare that they have no known competing financial interests or personal relationships that could have appeared to influence the work reported in this paper.

Acknowledgments

This research was partly supported by the EMPA POSTDOCS-II program that received funding from the European Union Horizon 2020 research and innovation program under the Marie Skłodowska-Curie grant agreement number 754364. The authors thank voestalpine BÖHLER Edelstahl GmbH & Co KG for providing the powder for the LPBF experiments. The authors (M.M and E.G) also gratefully acknowledges Prof. Mahmoud Nili-Ahmadabadi at Advanced Phase Transformation Laboratory, University of Tehran for providing TEM measurment.

REFERENCES

[1] Otsuka K, Wayman CM. Shape memory materials. 1st ed. Cambridge: University Press; 1999. p. 1–50.
[2] Rodrigue H, Wang W, Han M-W, Kim TJ, Ahn S-H. An overview of shape memory alloy-coupled actuators and robots. Soft Robot 2017;4(1):3–15.
[3] Cladera A, Weber B, Leinenbach C, Czaderski C, Shahverdi M, Motavalli M. Iron-based shape memory alloys for civil engineering structures: an overview. Construct Build Mater 2014;63:281–93.
[4] Ghafoori E, Hosseini E, Leinenbach C, Michels J, Motavalli M. Fatigue behavior of a Fe-Mn-Si shape memory alloy used for prestressed strengthening. Mater Des 2017;133:349–62.
[5] Mohri M, Taghizadeh M, Wang D, Hahn H, Nili-Ahmadabadi M. Microstructural study and simulation of intrinsic two-way shape memory behavior of functionally graded Ni-rich/NiTiCu thin film. Mater Char 2018;135:317–24.
[6] Khaleghi F, Tajally M, Emadoddin E, Mohri M. Functionally-graded shape memory alloy by diffusion annealing of palladium-coated NiTi plates. Met Mater Int 2017;23(5):915–22.
[7] Mohri M, Nili-Ahmadabadi M. Phase transformation and structure of functionally graded Ni–Ti bi-layer thin films with two-way shape memory effect. Sensor Actuator Phys 2015;228:151–8.
[8] Askari-Naeini FG, Taghizadeh M, Mohri M, Nili-Ahmadabadi M. On the microstructure and mechanical

properties of a two-way shape memory NiTi/NiTiCu bi-layer diaphragm. Mater Des 2020;188:108464.
[9] Janke L, Czaderski C, Motavalli M, Ruth J. Applications of shape memory alloys in civil engineering structures—overview, limits and new ideas. Mater Struct 2005;38(5):578–92.
[10] Tamai H, Kitagawa Y. Pseudoelastic behavior of shape memory alloy wire and its application to seismic resistance member for building. Comput Mater Sci 2002;25 (1):218–27.
[11] Sato A, Chishima E, Soma K, Mori T. Shape memory effect in $\gamma \rightleftarrows \varepsilon$ transformation in Fe-30Mn-1Si alloy single crystals. Acta Metall 1982;30(6):1177–83.
[12] Izadi M, Motavalli M, Ghafoori E. Iron-based shape memory alloy (Fe-SMA) for fatigue strengthening of cracked steel bridge connections. Construct Build Mater 2019;227:116800.
[13] Fritsch E, Izadi M, Ghafoori E. Development of nail-anchor strengthening system with iron-based shape memory alloy (Fe-SMA) strips. Construct Build Mater 2019;229:117042.
[14] Izadi M, Motavalli M, Ghafoori E. Thermally-activated shape memory alloys for retrofitting bridge double-angle connections. Eng Struct 2021;245:112827.
[15] Vůjtěch J, Ryjáček P, Matos JC, Ghafoori E. Iron-based shape memory alloy strengthening of a 113-years steel bridge. In: International conference on fibre-reinforced polymer (FRP) composites in civil engineering. Springer; 2021.
[16] Sawaguchi T, Nikulin I, Ogawa K, Sekido K, Takamori S, Maruyama T, Chiba Y, Kushibe A, Inoue Y, Tsuzaki K. Designing Fe–Mn–Si alloys with improved low-cycle fatigue lives. Scripta Mater 2015;99:49–52.
[17] Sawaguchi T, Sahu P, Kikuchi T, Ogawa K, Kajiwara S, Kushibe A, Higashino M, Ogawa T. Vibration mitigation by the reversible fcc/hcp martensitic transformation during cyclic tension–compression loading of an Fe–Mn–Si-based shape memory alloy. Scripta Mater 2006;54(11):1885–90.
[18] Dong Z, Klotz UE, Leinenbach C, Bergamini A, Czaderski C, Motavalli M. A novel Fe-Mn-Si shape memory alloy with improved shape recovery properties by VC precipitation. Adv Eng Mater 2009;11(1–2):40–4.
[19] Leinenbach C, Kramer H, Bernhard C, Eifler D. Thermo-mechanical Properties of an Fe–Mn–Si–Cr–Ni–VC shape memory Alloy with low transformation temperature. Adv Eng Mater 2012;14(1–2):62–7.
[20] Arabi-Hashemi A, Polatidis E, Smid M, Panzner T, Leinenbach C. Grain orientation dependence of the forward and reverse fcc ↔ hcp transformation in FeMnSi-based shape memory alloys studied by in situ neutron diffraction. Mater Sci Eng, A 2020;782:139261. https://doi.org/10.1016/j.msea.2020.139261.
[21] Koster M, Lee WJ, Schwarzenberger M, Leinenbach C. Cyclic deformation and structural fatigue behavior of an FE–Mn–Si shape memory alloy. Mater Sci Eng, A 2015;637:29–39.
[22] Heredia Rosa DI, Hartloper A, Sousa A, Lignos D, Motavalli M, Ghafoori E. Behavior of iron-based shape memory alloys under cyclic loading histories. In: The 5th international Conference on smart monitoring, Assessment and Rehabilitation of civil structures (SMAR 2019). Potsdam: Germany; 2019. 27 – 29 August.
[23] Koyama M, Sawaguchi T, Ogawa K, Kikuchi T, Murakami M. The effects of thermomechanical training treatment on the deformation characteristics of Fe–Mn–Si–Al alloys. Mater Sci Eng, A 2008;497(1–2):353–7.
[24] Matsumura O, Sumi T, Tamura N, Sakao K, Furukawa T, Otsuka H. Pseudoelasticity in an Fe–28Mn–6Si–5Cr shape memory alloy. Mater Sci Eng, A 2000;279(1–2):201–6.
[25] Khodaverdi H, Mohri M, Ghorabaei AS, Ghafoori E, Nili-Ahmadabadi M. Effect of low-temperature precipitates on microstructure and pseudoelasticity of an Fe–Mn–Si-based shape memory alloy. Mater Char 2023;195:112486.
[26] Leinenbach C, Arabi-Hashemi A, Lee W, Lis A, Sadegh-Ahmadi M, Van Petegem S, Panzner T, Van Swygenhoven H. Characterization of the deformation and phase transformation behavior of VC-free and VC-containing FeMnSi-based shape memory alloys by in situ neutron diffraction. Mater Sci Eng, A 2017;703:314–23.
[27] Arabi-Hashemi A, Lee W, Leinenbach C. Recovery stress formation in FeMnSi based shape memory alloys: impact of precipitates, texture and grain size. Mater Des 2018;139:258–68.
[28] Mohri M, Ferretto I, Leinenbach C, Kim D, Lignos DG, Ghafoori E. Effect of thermomechanical treatment and microstructure on pseudo-elastic behavior of Fe–Mn–Si–Cr–Ni-(V, C) shape memory alloy. Mater Sci Eng, A 2022;855:143917. https://doi.org/10.1016/j.msea.2022.143917.
[29] Khodaverdi H, Mohri M, Ghafoori E, Ghorabaei AS, Nili-Ahmadabadi M. Enhanced pseudoelasticity of an Fe–Mn–Si-based shape memory alloy by applying microstructural engineering through recrystallization and precipitation. J Mater Res Technol 2022;21:2999–3013. https://doi.org/10.1016/j.jmrt.2022.10.092.
[30] Chung C, Shuchuan C, Hsu T. Thermomechanical training behavior and its dynamic mechanical analysis in an Fe-Mn-Si shape memory alloy. Mater Char 1996;37(4):227–36.
[31] Khalil W, Saint-Sulpice L, Chirani SA, Bouby C, Mikolajczak A, Zineb TB. Experimental analysis of Fe-based shape memory alloy behavior under thermomechanical cyclic loading. Mech Mater 2013;63:1–11.
[32] W. Lee, B. Weber, G. Feltrin, M. Motavalli, and C. Leinenbach, Thermomechanical characterization of an Fe-Mn-Si-Cr-Ni-VC shape memory alloy for application in prestressed concrete structures. J Alloys Compd. 502.
[33] Baruj A, Bertolino G, Troiani H. Temperature dependence of critical stress and pseudoelasticity in a Fe–Mn–Si–Cr pre-rolled alloy. J Alloys Compd 2010;502(1):54–8.
[34] Gibson I, Rosen D, Stucker B, Khorasani M. Additive manufacturing technologies. Springer; 2014.
[35] Yintang W, Shuquan Z, Jiankang H, Qingliang Z, Bo L, Shifeng W. Four-dimensional printing——the additive manufacturing technology of intelligent components. J Mech Eng 2020;56:1–25.
[36] Kim D, Ferretto I, Leinenbach C, Lee W. 3D and 4D Printing of complex Structures of Fe- Mn- Si-based shape memory alloy using laser powder bed fusion. Adv Mater Interfac 2022;2022:2200171.
[37] A. Jafarabadi, 4D Printing of recoverable buckling-induced architected iron-based shape memory alloys. Addit Manuf, 2023. **: p. **.
[38] Yap CY, Chua CK, Dong ZL, Liu ZH, Zhang DQ, Loh LE, Sing SL. Review of selective laser melting: materials and applications. Appl Phys Rev 2015;2(4):41101.
[39] Mehrpouya M, Gisario A, Nematollahi M, Rahimzadeh A, Baghbaderani KS, Elahinia M. The prediction model for additively manufacturing of NiTiHf high-temperature shape memory alloy. Mater Today Commun 2021;26:102022 (1–8).
[40] Mehrpouya M, Gisario A, Rahimzadeh A, Nematollahi M, Baghbaderani KS, Elahinia M. A prediction model for finding the optimal laser parameters in additive manufacturing of NiTi shape memory alloy. Int J Adv Des Manuf Technol 2019;105(11):4691–9.
[41] Niendorf T, Brenne F, Krooß P, Vollmer M, Günther J, Schwarze D, Biermann H. Microstructural evolution and functional properties of Fe-Mn-Al-Ni shape memory alloy processed by selective laser melting. Metall Mater Trans 2016;47(6):2569–73.

[42] Ewald FC, Brenne F, Gustmann T, Vollmer M, Krooß P, Niendorf T. Laser powder bed fusion processing of Fe-Mn-Al-Ni shape memory alloy—on the effect of elevated platform temperatures. Metals 2021;11(2):185.
[43] Ferretto I, Kim D, Della Ventura N, Shahverdi M, Lee W, Leinenbach C. Laser powder bed fusion of a Fe–Mn–Si shape memory alloy. Addit Manuf 2021;46:102071.
[44] Ferretto I, Borzì A, Kim D, Ventura NMD, Hosseini E, Lee WJ, Leinenbach C. Control of microstructure and shape memory properties of a Fe-Mn-Si-based shape memory alloy during laser powder bed fusion. Additive Manufacturing Letters 2022;3:100091.
[45] Ferretto I, Kim D, Mohri M, Ghafoori E, Lee WJ, Leinenbach C. Shape recovery performance of a (V, C)-containing Fe–Mn–Si–Ni–Cr shape memory alloy fabricated by laser powder bed fusion. J Mater Res Technol 2022;20:3969–84.
[46] Kim D, Ferretto I, Jeon JB, Leinenbach C, Lee W. Formation of metastable bcc-δ phase and its transformation to fcc-γ in laser powder bed fusion of Fe–Mn–Si shape memory alloy. J Mater Res Technol 2021;14:2782–8.
[47] Yang Y, Arabi-Hashemi A, Leinenbach C, Shahverdi M. Influence of thermal treatment conditions on recovery stress formation in an FeMnSi-SMA. Mater Sci Eng, A 2021;802:140694.
[48] Ferretto IK, Dohyung, Mohri M, Ghafoori E, Lee W, Leinenbach C. Enhanced pseudo-elasticity in a VC-containing iron-based shape memory alloy fabricated by laser powder bed fusion. Mater Des 2022;2022.
[49] Bracke L, Kestens L, Penning J. Transformation mechanism of α′-martensite in an austenitic Fe–Mn–C–N alloy. Scripta Mater 2007;57(5):385–8.
[50] Nikulin I, Sawaguchi T, Yoshinaka F, Takamori S. Influence of cold rolling deformation mechanisms on the grain refinement of Fe–15Mn–10Cr–8Ni–4Si austenitic alloy. Mater Char 2020;162:110191 (1–13).
[51] Kempf A, Hilgenberg K. Influence of sub-cell structure on the mechanical properties of AlSi10Mg manufactured by laser powder bed fusion. Mater Sci Eng, A 2020;776:138976.
[52] Zitelli C, Folgarait P, Di Schino A. Laser powder bed fusion of stainless steel grades. a review. Metals 2019;9(7):731.
[53] Criales LE, Arısoy YM, Lane B, Moylan S, Donmez A, Özel T. Laser powder bed fusion of nickel alloy 625: experimental investigations of effects of process parameters on melt pool size and shape with spatter analysis. Int J Mach Tool Manufact 2017;121:22–36.
[54] DebRoy T, Wei H, Zuback J, Mukherjee T, Elmer J, Milewski J, Beese AM, Wilson-Heid Ad, De A, Zhang W. Additive manufacturing of metallic components–process, structure and properties. Prog Mater Sci 2018;92:112–224.
[55] Köhnen P, Létang M, Voshage M, Schleifenbaum JH, Haase C. Understanding the process-microstructure correlations for tailoring the mechanical properties of L-PBF produced austenitic advanced high strength steel. Addit Manuf 2019;30:100914.
[56] Lai M, Li Y, Lillpopp L, Ponge D, Will S, Raabe D. On the origin of the improvement of shape memory effect by precipitating VC in Fe–Mn–Si-based shape memory alloys. Acta Mater 2018;155:222–35.
[57] Kajiwara S. Characteristic features of shape memory effect and related transformation behavior in Fe-based alloys. Mater Sci Eng, A 1999;273:67–88.
[58] Bergeon N, Kajiwara S, Kikuchi T. Atomic force microscope study of stress-induced martensite formation and its reverse transformation in a thermomechanically treated Fe–Mn–Si–Cr–Ni alloy. Acta Mater 2000;48(16):4053–64.
[59] Lee W, Weber B, Feltrin G, Czaderski C, Motavalli M, Leinenbach C. Phase transformation behavior under uniaxial deformation of an Fe–Mn–Si–Cr–Ni–VC shape memory alloy. Mater Sci Eng, A 2013;581:1–7.
[60] Chen Y, Burgess T, An X, Mai Y-W, Tan HH, Zou J, Ringer SP, Jagadish C, Liao X. Effect of a high density of stacking faults on the Young's modulus of GaAs nanowires. Nano Lett 2016;16(3):1911–6.
[61] Over H, Knotek O, Lugscheider E. Elastic properties of silicon single crystals in dependence on temperature and dislocation density. Z Metallkd 1982;73(9):552–7.
[62] Pan M-M, Zhang X-M, Zhou D, Misra R, Chen P. Fe–Mn–Si–Cr–Ni based shape memory alloy: Thermal and stress-induced martensite. Mater Sci Eng, A 2020;797:140107.